Blind source separation for clutter and noise suppression in ultrasound imaging

Blind Source Separation for Clutter and Noise Suppression in Ultrasound Imaging: Review for Different Applications

R. R. Wildeboer, F. Sammali, R. J. G. van Sloun, Y. Huang, P. Chen, M. Bruce, C. Rabotti, S. Shulepov, G. Salomon, B. C. Schoot, H. Wijkstra, and M. Mischi

***Abstract*— Blind source separation (BSS) refers to a number of signal processing techniques that decompose a signal into several "source" signals. In recent years, BSS is increasingly employed for the suppression of clutter and noise in ultrasonic imaging. In particular, its ability to separate sources based on measures of independence rather than their temporal or spatial frequency content makes BSS a powerful filtering tool for data in which the desired and undesired signals overlap in the spectral domain. The purpose of this work was to review the existing BSS methods and their potential in ultrasound imaging. Furthermore, we tested and compared the effectiveness of these techniques in the field of contrast-ultrasound super-resolution, contrast quantification, and speckle tracking. For all applications, this was done *in silico*, *in vitro*, and *in vivo*. We found that the critical step in BSS filtering is the identification of components containing the desired signal and highlighted the value of *a priori* domain knowledge to define effective criteria for signal component selection.**

***Index Terms*— Blind source separation (BSS), contrast-enhanced ultrasound, independent component analysis (ICA), microbubbles, nonnegative matrix factorization (NMF), principal component analysis (PCA), speckle tracking (ST), super-resolution, singular value decomposition (SVD), ultrasound imaging.**

Manuscript received December 21, 2019; accepted February 17, 2020. Date of publication February 20, 2020; date of current version July 24, 2020. This work was supported in part by the IMPULS2 Program within the Eindhoven University in collaboration with Philips, in part by an unrestricted grant from the Dutch Cancer Society under Grant UVA2013-5941 and in part by a Starting Grant from the European Research Council under Grant 280209, in part by the Dutch TTW under Grant HTSM-13901, in part by Ferring, in part by SuperSonic Imagine, and in part by Samsung. *(Corresponding author: R. R. Wildeboer.)*

R. R. Wildeboer, F. Sammali, R. J. G. van Sloun, Y. Huang, P. Chen, C. Rabotti, and M. Mischi are with the Laboratory of Biomedical Diagnostics, Department of Electrical Engineering, Eindhoven University of Technology, 5612 AZ Eindhoven, The Netherlands (e-mail: r.r.wildeboer@tue.nl; f.sammali@tue.nl; r.j.g.v.sloun@tue.nl).

M. Bruce is with the Applied Physics Laboratory, University of Washington, Seattle, WA 98195 USA.

S. Shulepov is with Philips Research, 5656 AE Eindhoven, The Netherlands.

G. Salomon is with the Martini Klinik–Prostate Cancer Center, University Hospital Hamburg-Eppendorf, 20246 Hamburg, Germany.

B. C. Schoot is with the Department of Obstetrics and Gynecology, Catharina Hospital, 5623 EJ Eindhoven, The Netherlands, and also with University Hospital Ghent, 9000 Ghent, Belgium.

H. Wijkstra is with the Laboratory of Biomedical Diagnostics, Department of Electrical Engineering, Eindhoven University of Technology, 5612 AZ Eindhoven, The Netherlands, and also with the Department of Urology, Amsterdam University Medical Centers, University of Amsterdam, 1105 AZ Amsterdam, The Netherlands.

This article has supplementary downloadable material available at http://ieeexplore.ieee.org, provided by the author.

Digital Object Identifier 10.1109/TUFFC.2020.2975483

I. Introduction

In RECENT years, increasingly advanced algorithms have been developed to analyze ultrasonic (US) acquisitions, from the generation of super-resolution images revealing vascular structures beyond the diffraction limit [1], [2] to the distinct extraction of time-intensity curves (TICs) in the cardiac system or well-perfused organs [3], [4] up to dedicated speckle-tracking (ST) algorithms to estimate strain [5], [6] in, e.g., the heart, arteries, and uterus. The gravity of data preprocessing should not be overlooked when appreciating the impressive results obtained by these methods. Particularly in clinical application, US data are often obscured by prevalent clutter sources, artifacts can arise due to patient or operator motion, and noise levels may well exceed those in laboratory conditions. Therefore, robust filtering is needed to separate the desired signal(s) from the undesired signals prior to further analysis.

Traditionally, clutter and noise suppression in US recordings is performed with temporal filters (e.g., for clutter removal [7]) and spatial filters (e.g., for despeckling [8], [9]). Infinite response filter (IIR) and finite impulse response filter (FIR) as well as regression filters have been widely applied for this purpose [7], [10]–[16]. These filters rely on the assumption that the temporal or spatial frequency content of clutter, noise, and the signal of interest is distinctly different [14]–[16]. This assumption is not always valid; there is thus a real risk of losing useful information or failing to remove signals that affect the performance of the algorithms used for, e.g., super-resolution and ST.

In this respect, blind source separation (BSS) techniques have been receiving more and more attention. Unlike the aforementioned filters, BSS techniques decompose data into underlying "sources" or components. Components corresponding to clutter or noise sources are subsequently discarded. Particularly in blood flow imaging [14], [16]–[18] and, more recently, ultrasound super-resolution imaging [19]–[21], BSS is increasingly applied. The identification of the clutter and

signal components is a relevant aspect for several applications. Although thresholds might be heuristically or empirically established, signal content can vary from application to application, between different acquisitions, or even within the same acquisition over time. In that respect, generalizable, adaptive filtering is something to aim for [14], [17].

The purpose of this work was to review, evaluate, and compare several existing BSS methods as well as a wide range of (recently proposed as well as novel) adaptive criteria for clutter and noise suppression in US imaging. The implementation of BSS may be different from application to application. To highlight important considerations, we tailored the BSS filtering to three fields of interest as an example: 1) super-resolution by US localization microscopy; 2) contrast-enhanced US (CEUS) quantification by TIC analysis, and 3) US ST. As BSS in Doppler imaging has been most studied, we refer to some excellent articles on this subject for a treatise on effective BSS implementation in blood flow imaging [14], [16]–[18].

Albeit the three included applications are ultrasound-based, generally very different features in the US videos are regarded as undesired. For example, while speckles are considered noise in contrast ultrasound, they are essential to ST. However, as these application fields are very broad, we only refer to the key articles of each application and focus more in-depth on the implementation of adaptive BSS filtering. In this way, we provide the reader with some guidelines for custom BSS filter design in ultrasound imaging.

This article is organized as follows. In Section II, the theoretical framework of BSS is introduced and discussed. Section III elaborates on the use of BSS for the adaptive filtering of ultrasound data. Together, these sections provide a general framework for the different strategies and implementations of dedicated US filtering that will be discussed and tested for the three different US applications. This is described in Section IV. Finally, the results are discussed in Section V and conclusions are drawn in Section VI.

II. Theoretical Framework and (Blind) Source Separation Methods

A. Fundamentals of (Blind) Source Separation

Irrespective of the US imaging technique used, the relevant information is to some extent distorted or obscured by undesired signals [22]–[24]. In this work, we strive to specifically separate the desired signal from noise (i.e., random distortions of the signal—lectronic noise), clutter (i.e., undesired, deterministic sources from the measurement space—tissue movement and multiplicative (speckle) noise), and artifacts (i.e., signal distortions caused by the operator, patient, or external structures—motion artifacts and shadowing).

As we are interested in dynamic US acquisitions throughout this article, we will refer to our observed signal using the Casorati matrix $\mathbf{X}$ of size $N_s \times N_t$, with all our spatial dimensions condensed in the rows (i.e., $N_s = N_x \cdot N_y$) and our temporal dimension distributed over the columns. $\mathbf{X}$ will be a mix of all abovementioned sources. For BSS, we assume that this mixing process occurs through linear combination

$$\mathbf{X} = \mathbf{X}_{\text{signal}} + \mathbf{X}_{\text{noise}} + \mathbf{X}_{\text{clutter}} + \mathbf{X}_{\text{artefact}}. \tag{1}$$

When filtering, we aim to maximize our signal-to-noise ratio (SNR) by removing the undesired sources mixed into our observed image $\mathbf{X}$. This procedure is often based on signal decomposition or basis transformation, that is, the mapping of the signal onto new bases that will enable discrimination and identification of the sources that make up the signal. When appropriate bases are found, a filtered output image is readily generated by transforming only a (weighted) subset of distinct signal components back to the image space.

Traditionally, *a priori* knowledge of the signal and undesired sources is used to determine the basis onto which $\mathbf{X}$ will be projected. A widely used example of such a strategy is frequency filtering, where the sampled signals are transformed to the frequency domain through discrete Fourier transformation (DFT). When the spectral characteristics of the desired signal or, alternatively, the undesired signals (e.g., high-frequency noise or interference by the power mains) are known, a filtered image can be reconstructed by disregarding specific frequency components. Spatial filters (e.g., smoothing) work essentially in a similar fashion, filtering out undesired spatial frequencies. In many applications, however, the desired and undesired signals may be present in the same (spatial) frequency bands, rendering the DFT strategy insufficient [7], [14], [16], [25]. The same holds for other nonblind transformations, such as the discrete wavelet transformation often used in despeckling strategies [8].

Another approach would be to determine the basis transformation adaptively, that is, depending on the signal statistics themselves. As we do not need prior information on the sources underlying our observations or how the mixture is formed, we refer to this strategy as BSS [23], [26]. Filtering is then a three-step process, consisting of finding the bases that provide the best separation of sources, identifying the components that should subsequently be (partially) removed from the signal, and mapping the remaining signal back to its original domain [25]. In this section, the first and last steps will be discussed; the second step will be treated in Section III.

B. Discrete Fourier Analysis

DFT is perhaps the most common form of non-BSS, where $\mathbf{X}$ is decomposed into several frequency bands (in this case, these are the "sources"). In the matrix form, the inverse DFT reads

$$\mathbf{X}^T = \mathbf{W}_{\text{DFT}}^{-1}\mathbf{Y}^T \tag{2}$$

where $\mathbf{Y}$ is a complex $N_s \times N_t$ matrix containing the magnitude and phase of every frequency component in each pixel and $\mathbf{W}_{\text{DFT}}$ is the $N_t \times N_t$ DFT matrix [27]

$$\mathbf{W}_{\text{DFT}} = \frac{1}{N_t}\begin{bmatrix} 1 & 1 & \cdots & 1 \\ 1 & e^{\frac{-j2\pi}{N_t}} & \cdots & e^{\frac{-j2\pi(N_t-1)}{N_t}} \\ 1 & e^{\frac{-j4\pi}{N_t}} & \cdots & e^{\frac{-j4\pi(N_t-1)}{N_t}} \\ \vdots & \vdots & \ddots & \vdots \\ 1 & e^{\frac{-j2\pi(N_t-1)}{N_t}} & \cdots & e^{\frac{-j2\pi(N_t-1)^2}{N_t}} \end{bmatrix}. \tag{3}$$

No information is lost during the procedure, and the image can be fully restored through its inverse transformation. We refer to this as lossless. For comparison with BSS methods, we show that the representation of an individual frequency component k can be isolated through multiplication of the kth column of matrix $\mathbf{Y}$ and the kth column of the inverse DFT matrix

$$\mathbf{X}_k^T = \mathbf{w}_{\mathrm{DFT},k}^{-1}\mathbf{y}_k^T. \tag{4}$$

In the same way, by not using the transposed version of $\mathbf{X}$, spatial frequencies can be assessed. In the remainder of this article, however, we primarily focus on temporal frequencies.

C. Singular Value Decomposition

As said, in contrast to DFT where the bases are defined *a priori*, BSS infers them from the signal itself. One of the most frequently used BSS techniques is singular value decomposition (SVD), a generalization of eigendecomposition that decomposes any matrix $\mathbf{X}$ as [28]

$$\mathbf{X} = \mathbf{U}\Sigma\mathbf{V}^T \tag{5}$$

where $\mathbf{U}$ is an $N_s \times N_s$ unitary matrix (i.e., orthogonal for real-valued inputs), Σ is an $N_s \times N_t$ pseudodiagonal matrix containing the singular values σ as diagonal elements, conventionally in descending order, and $\mathbf{V}$ is an $N_t \times N_t$ unitary matrix. The columns in $\mathbf{V}$ can be viewed to contain the singular vectors carrying the temporal information corresponding to spatial information in the column vectors of $\mathbf{U}$. Accordingly, we have separated $k = \min(N_s, N_t)$ sources that can be retrieved through

$$\mathbf{X}_k = \sigma_k \mathbf{u}_k \mathbf{v}_k^T. \tag{6}$$

Statistically, we have now decomposed our data into orthogonal subspaces. The vectors $\mathbf{u}_k$ in $\mathbf{U}$ and $\mathbf{v}_k$ in $\mathbf{V}$ correspond to the eigenvalues of the autocovariance matrix of $\mathbf{X}$ [29] and, therefore, intrinsically provide a basis with maximum covariance. In fact, according to the Eckart–Young theorem [30], a partial SVD provides the lowest rank approximation of $\mathbf{X}$ of all low-rank matrices and therefore, by definition, equals or outperforms DFT in effectively decomposing $\mathbf{X}$ [14], [31]. Although Σ is unique, its singular vectors are not. The numerical algorithms to find the SVD are usually based on (QR) bidiagonalization and Jacobi methods [32], of which the first is the most popular [33].

Furthermore, while SVD and DFT (see equation [2]) create an orthonormal temporal basis (i.e., $\mathbf{W}_{\mathrm{DFT}}$ and $\mathbf{V}^T$, respectively), the spatial vectors in $\mathbf{Y}$ are not, by definition, orthogonal as is $\mathbf{U}\Sigma$. Interestingly, Demené *et al.* [14] showed that for their US data, the high singular vectors were associated with low-frequency and low singular vectors with high-frequency temporal signals. This is a consequence of the small (tissue-related) movements being more spatiotemporally coherent in blood flow imaging rather than a general rule; however, similar behavior can be observed in many US applications. On the other hand, for example, Sammali *et al.* [34] found the frequency of periodic uterine contractions (and its harmonics) in the first few singular components as these make up the most dominant spatiotemporally coherent signals.

D. Principal Component Analysis

SVD methods are often presented in the framework of principal component analysis (PCA), a widely used method for dimensionality reduction, decomposing an image into a new orthogonal representation that retains maximum covariance. There are several ways to perform PCA [35], but the simplest might be an eigendecomposition of the sample autocovariance matrix, as can be estimated from the data. However, in this work, we will refer to PCA only if the orthogonal axes are also maximally decorrelated. When each column in $\mathbf{X}$ is centered (i.e., has a mean of zero) and standardized (i.e., has a standard deviation of 1), the autocovariance matrix translates into the autocorrelation matrix $\mathbf{R}$. As such, PCA is also referred to as the Karhunen–Loève transform [15], [36]. Decorrelation can now be performed through eigendecomposition of the (square and symmetric) sample autocorrelation matrix

$$\mathbf{R} = \mathbf{X}^T\mathbf{X} = \mathbf{V}\Lambda\mathbf{V}^T \tag{7}$$

where, similar to SVD, Λ contains the eigenvalues λ in descending order along the diagonal and the matrix $\mathbf{V}$ contains the temporal eigenvectors as columns, that is, the principal components. In fact, SVD can be exploited to perform PCA without having to perform eigendecomposition. Since $\mathbf{V}$ and $\mathbf{U}$ are unitary matrices

$$\mathbf{R} = \mathbf{X}^T\mathbf{X} = \mathbf{V}\Sigma^T\mathbf{U}^T\mathbf{U}\Sigma\mathbf{V}^T = \mathbf{V}\Sigma^2\mathbf{V}^T. \tag{8}$$

Accordingly, the eigenvalues of the autocorrelation matrix in time (or similarly, in transposed form, in space) are related to the singular values through

$$\lambda_k = \sigma_k^2. \tag{9}$$

Following 5, the spatial distribution of the principal components can be retrieved through $\mathbf{U} = \mathbf{X}\mathbf{V}\Sigma^{-1}$. Therefore, after centerization and standardization, one can perform ordinary SVD and retrieve the individual principal components through 6. Subsequently, these components form the original image when multiplied with the former standard deviations and added to the mean that was retracted previously.

E. Robust Principal Component Analysis

Rather than solely using the autocovariance or correlation to decompose data, robust PCA (RPCA) actively promotes sparsity in the decomposition process. This low rank plus sparse methodology known as RPCA [41], implemented in MRI [42]–[44] and, more recently, in ultrasound [45]–[47], separates sparse and low-rank (highly coherent) elements in an alternating two-step fashion so that

$$\min(||\mathbf{L}|| + l_1||\mathbf{S}||_1), \quad \text{s.t. } \mathbf{L} + \mathbf{S} = \mathbf{X} \tag{10}$$

where $\mathbf{L}$ and $\mathbf{S}$ are the low-rank and sparse component matrices, respectively [41].

Depending on the nature of the (un)desired signals, the inclusion of the l_1-norm in the cost function further minimizes the remaining overlap of signal and clutter in the SVD components. However, when the clutter or the noise sources are not necessarily considered sparse, this approach does not improve upon SVD itself other than the sparse rejection of potential outliers.

F. Independent Component Analysis

In the thus far described BSS techniques, the desired and undesired signals are assumed to principally end up in distinct subspaces. Independence between the components is promoted by requiring them to be orthogonal and of maximum autocovariance. However, orthogonality does not necessarily indicate that the components are mutually independent and orthogonal axes might therefore not fully separate the different sources [15].

As opposed to eigendecomposition-related techniques, independent component analyses (ICAs) decompose signals by assuming linear independence between the sources mixed into the observed signal [48]. Often, ICA techniques iteratively maximize the non-Gaussianity of N_n sources. This originates from the underlying concept that, as the central limit theorem states that the sum of independent random variables grows toward a Gaussian distribution, independent sources can be identified by their deviation from this Gaussianity.

There is a wide range of possible cost functions ensuring non-Gaussianity, of which kurtosis, (neg)entropy, and mutual information are most employed [49], [50]. The kurtosis is easily implementable but often more sensitive to outliers. Negentropy, on the other hand, is a less sensitive, information-theory-based estimator of non-Gaussianity, but it is computationally difficult to implement as it depends on, e.g., sample counting or kernel-density estimation [49]. Therefore, the negentropy is often approximated rather than fully calculated. For both cost functions, the data need to be centered and standardized prior to analysis. Often the data are also whitened [51] so that signal components are uncorrelated such as in PCA and the ICA problem is simplified. For uncorrelated, unit-variance data, the negentropy and mutual information differ only by a constant [49].

For ICA with N_n sources, it is assumed that components in an $N_n \times N_s$ source matrix $\mathbf{S}$ are linearly mixed into the observed signal by an $N_t \times N_n$ mixing matrix $\mathbf{W}_{\text{ICA}}$ following:

$$\mathbf{X}^T = \mathbf{W}_{\text{ICA}}\mathbf{S} + \mathbf{N}^T \tag{11}$$

where $\mathbf{N}$ is the residual noise matrix, resulting from ICA not being lossless. In this formulation, the temporal independence between the bases vectors is promoted; likewise, a transposed Casorati matrix formulation of the ICA procedure would yield spatial independence [52]. Choosing the number of independent sources N_n is not a trivial problem; it might be determined in an iterative fashion [53], by data reduction through, e.g., SVD prior to analysis [52] or using information theoretic criteria [54] (see Section III-1).

Once the number of sources is established, the unknown matrices $\mathbf{W}_{\text{ICA}}$ and $\mathbf{S}$ can be approximated, for instance, using the often used fast ICA fixed-point iteration algorithm proposed by Hyvärinen [55]. Other methods include the joint approximate diagonalization eigenmatrices (JADEs) [56], [57] and Information-Maximization (InfoMax) algorithms [58]. Finally, in line with the other methods, also ICA allows the extraction of individual components by multiplication of the kth column of matrix $\mathbf{W}_{\text{ICA}}$ and the kth row of matrix $\mathbf{S}$

$$\mathbf{X}_k = \mathbf{w}_{\text{ICA},k}\mathbf{s}_k. \tag{12}$$

The order of the independent sources in $\mathbf{S}$ depends on the initialization of the iterative procedure. However, the sources can readily be arranged in descending order of the discrete-time signal energy (i.e., $E_k = \mathbf{s}_k^T\mathbf{s}_k$), provided that the corresponding columns in $\mathbf{W}_{\text{ICA}}$ all have the same energy [49]. In contrast to PCA and SVD, the ICA-decomposed subspaces are not necessarily orthogonal.

When the desired and undesired sources are indeed independent, ICA generally achieves more accurate separation [59]. This is likely the case for additive noise and some distinct sources of clutter and artifacts. However, some other noise sources can be very much interdependent with the desired signal: for example, multiplicative noise or the relation between blood flow and wall motion [15]. Moreover, though $\mathbf{W}_{\text{ICA}}$ is assumed stationary in this ICA approach, the mixing may be considerably time variant (i.e., nonstationary) [60].

G. Nonnegative Matrix Factorization

Another BSS approach is nonnegative matrix factorization (NMF). This method does not impose independence, orthogonality, or maximum covariance, but it aims to decompose the observations $\mathbf{X}$ into a nonnegative $N_s \times N_n$ basis matrix $\mathbf{W}_{\text{NMF}}$ and an $N_n \times N_t$ nonnegative encoding matrix $\mathbf{H}$ given a certain cost function [61], [62]

$$\mathbf{X} = \mathbf{W}_{\text{NMF}}\mathbf{H} + \mathbf{N}. \tag{13}$$

Because also NMF is lossy, 13 contains a residual noise matrix $\mathbf{N}$. Similar to the other methods, individual components can be retrieved by multiplication of the kth column and kth row of $\mathbf{W}_{\text{NMF}}$ and $\mathbf{H}$

$$\mathbf{X}_k = \mathbf{w}_{\text{NMF},k}\mathbf{h}_k. \tag{14}$$

There are a number of NMF algorithms available that range from basic NMF decomposition to those with a structured factorization or additional constraints such as sparsity or orthogonality [63]. The alternating least squares and the multiplicative update algorithm are most used, of which the first was chosen for this work.

An advantage of NMF is that the nonnegativity constraint leads to more physically intuitive bases than, for instance, ICA and PCA [61]. Even though ultrasound images cannot contain negative values, the bases found by the latter two methods usually have abundant negative values that cancel out when linearly combined to form the original image. In contrast, being nonnegative by definition, the NMF-bases in $\mathbf{W}_{\text{NMF}}$ generally have more physical correspondence to the sources underlying $\mathbf{X}$ [62].

III. Adaptive Filtering

Now, we turn to examine how BSS filtering strategies (as summarized in Table I) can be tailored to a US application. An essential step is the identification of the signal components. There are three approaches to select the appropriate subset of the desired components: empirically per acquisition or application (see [20], [64]–[69]), experimentally optimized per acquisition (see [14], [21]), or adaptively based on the

TABLE I
DETAILS OF (BLIND) SOURCE SEPARATION METHODS FOR US APPLICATION

method	blind-ness	pre-processing	cost function	properties	inverti-bility	computational complexity*	compt'n time**
Discrete Fourier Transform	*a priori*	-	-	orthogonal	lossless	$\mathcal{O}(N_t \log_2 N_t)$ [37]	1.12 s
Singular Value Decomposition	blind	-	autocovariance	orthogonal	lossless	$\mathcal{O}(\min(N_s^2 N_t, N_s N_t^2))$ [38]	0.62 s
Principal Component Analysis	blind	cent'd/stand'd	autocorrelation	orthogonal	lossless	$\mathcal{O}(\min(N_s^2 N_t, N_s N_t^2))$ [38]	0.79 s
Independent Component Analysis	blind	cent'd/stand'd	kurtosis	-	lossy	$\mathcal{O}(\max(N_s^2 k, N_t^2 k))$ [39]	0.79 s
Non-negative Matrix Factorisation	blind	-	RMS residual	-	lossy	$\mathcal{O}((N_s N_t)^{k^2})$ [40]	20 s

** order of computational cost for most common algorithms; **for comparison, decomposition time for the ULM simulation in Section IV.*

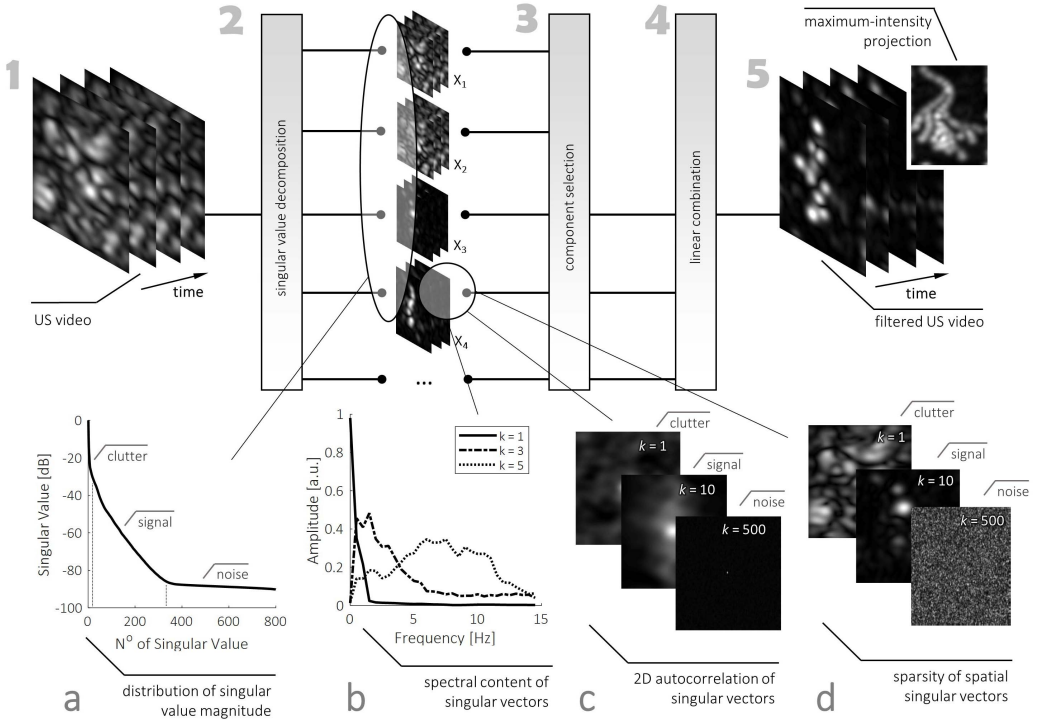

Fig. 1. Schematic of a BSS filtering strategy for super-resolution imaging, depicting (1) the original data, (2) SVD, (3) component selection, (4) linear combination of the remaining components, and (5) the filtered data. Component selection might be based on (a) distribution of the singular vectors, (b) spectral content of the temporal singular vectors, (c) autocorrelation within the spatial singular vectors, or (d) sparsity model of the spatial components.

characteristics of the components (see [16]–[18], [25], [34], [70]–[73]).

For the first two methods, respectively, a specific subset of components is defined manually or by experimentally maximizing specific quality measures such as the contrast-to-noise ratio (CNR). The adaptive approach is generally more robust and generalizable since it does not rely on qualitative assessment of decomposition characteristics, which may differ considerably across acquisitions. Several adaptive criteria for component selection have been proposed in recent years. Traditionally, information-theoretic criteria have been used for dimensionality reduction and, thus, for pruning the noise components from the signal. As these criteria are not able to identify the undesired but deterministic clutter signals, also approaches based on, e.g., each component's spectral content, spatial similarity, eigenvalue, or singular value distribution have been considered (see Fig. 1 for a schematic of the filtering paradigm and Table II for an overview of approaches).

1) Information Theory: An advantage of information-theoretic criteria for component selection is in that they do not rely on user-set thresholds; we consider only the components that are theoretically necessary to carry the information of our image and, consequently, regard the other components as noise. The optimal number of components arises as a tradeoff between an as large as possible descriptive power (i.e., high log-likelihood) and an as low as possible model complexity (i.e., a low number of components). There are several ways to weight this tradeoff, of which the minimum description length [78] and Akaike's information criterion (AIC) [79] are the most common, that is [54], [80]

$$E_{\mathrm{MDL}}(k) = -L(k) + \frac{1}{2}(k(2N_k - k))\log(N_t) \quad (15)$$

$$E_{\mathrm{AIC}}(k) = -2L(k) + 2(k(2N_k - k)) \quad (16)$$

TABLE II
FILTERING APPROACHES FOR BSS COMPONENT SELECTION

Approach	**Criterium**	**Domain Knowledge***	*Super-Resolution*	*Speckle Tracking*	*TIC Modelling*
Empirical	Arbitrary Subset of Components [20], [64]–[69]				
Experimental	Maximum CNR [14], [21], [74]				
Information Theory	Minimum Description Length•	N/A	-	-	-
	Akaike's Information Criterion•	N/A	-	-	-
Noise Modelling	Marčenko-Pastur Noise• [18]	N/A	-	-	-
	Singular Curve Slope• [25]	$[\sigma_{k+1}/\sigma_k]_c$	> 0.99	> 0.99	> 0.99
	Cumulative Percent Variance• [17]	$\mathrm{Var}[\mathbf{X}_k]_c$	$> 99.9\%$	$> 90\%$	$> 20\%$
	Average Eigenvalue• [70]	N/A	-	-	-
	Spatiotemporal Entropy•	N/A	-	-	-
Component Energy	Singular Value Magnitude• [16], [25], [73]	σ_c; λ_c	1	$\sim 10^{10}$; $\sim 10^7$	-
	Relative Singular Magnitude• [17]	σ_c [dB]	> -20 dB	h> -55 dB u> -100 dB	> -20 dB
	Singular Curve Turning Point• [17]	N/A	-	-	-
Spectral Content	Spectral Power Density [17], [25], [34]	f_c	$>$ 10, 12, 25 Hz$^+$	h: 0.5$-$1.5 Hz u: 0.04$-$0.06 Hz	$<$ 0.15 Hz [75]
Spatial Coherence	2D Autocorrelation	2D FWHM$_c$	$<$ 0.13-mm	h$>$0.21-mm u$>$0.24-mm	$>$ 0.5-mm [76]
	Spatial Frequency Spectrum	ξ_c	> 3.3 mm^{-1}	h<0.1 mm^{-1} u<0.5 mm^{-1}	< 0.75 mm^{-1}
	Spatial Similarity Matrix [17], [71], [72]	N/A	-	-	-
Model Fitting	Goodness-of-fit	model; ϵ_c	Sparsity $\hat{\kappa}_4$ [77]	Periodicity	LDRW [4]

• = SVD / PCA only; *$[\cdot]_c$ = cut-off value; $^+$for the *in-silico*, *in-vitro*, and *in-vivo* data; h = heart; u = uterus

where N_k is the number of components and $L(k)$ is the log-likelihood function. For SVD and PCA, Wax and Kailath [80] formulated a description of the log likelihood based on the eigenvalues

$$L(k) = \log\left(\frac{\prod_{i=k+1}^{N_k} \lambda_i^{1\backslash(N_k-k)}}{\frac{1}{N_k-k}\sum_{i=k+1}^{N_k}\lambda_i}\right)^{(N_k-k)N_t}. \tag{17}$$

To apply information-theoretic filtering, we include only the first k components, where k minimizes either $E_{\mathrm{MDL}}(k)$ or $E_{\mathrm{AIC}}(k)$, a method that has been proven useful for subspace selection in, e.g., contrast-ultrasound velocity imaging [81]. For ICA and NMF, on the other hand, the number of sources (i.e., components) is predefined. It has been proposed to use the MDL and AIC criteria to determine the number of (independent) sources that have to be assumed for the best description of the data [54].

2) Noise Modeling: Instead of selecting the components that contain signals, we could also identify those that contain noise. Again, for ICA and NMF, the number of sources should be chosen such that noise-containing components are avoided. For SVD and PCA, however, a majority of the components will predominately consist of noise. As described by Marčenko and Pastur [82], a random matrix will have a set of eigenvalues that log-linearly decreases in value. This fact can be exploited by identifying the component number after which the eigenvalues start decreasing linearly in the log domain [18].

In a more pragmatic implementation of this principle, Yu and Lovstakken [25] described noise removal from Doppler acquisitions by excluding components with an eigenvalue that is too similar to the previous one ($\lambda_k/\lambda_{k-1} \approx 1$). Alternatively, one could also exclude those components of which the eigenvalues only explain the remaining amount of variance (i.e., restricting the cumulative percentage variance (CPV) [17], [70]) or those of which the eigenvalue is below the average eigenvalue [70]. Finally, examining the spatiotemporal entropy of each component [83], one can appreciate that signal and noise components usually occupy a low-entropy and a high-entropy domain, respectively.

3) Signal Energy: Unfortunately, the two aforementioned approaches are only designed to separate (white) noise from deterministic signals. To remove clutter signals from a recording, we should take a closer look at our component characteristics. In fact, closely related to the previous approach, one could assume that clutter, signal, and noise differ in their contribution to the signal energy. In flow imaging, for example, the strongest signals are usually associated with clutter and the lowest with noise [14], [17], [65].

For ICA and NMF, each component's signal energy could be considered. In SVD and PCA, the removal of the strongest components is easiest by examining the eigenvalues and (partially) rejecting those above a certain cutoff ($\lambda_k > \lambda_c$) [16], [25]. Another approach is to examine the slope of the singular value distribution and defining different regimes

that are associated with clutter, signal, and noise [17]. Here, the "turning points" in the singular curve defined by local minima in the curvature radius mark the transition between the regimes.

4) Spectral Content: Another way to separate clutter and noise from the desired signal is by investigating each component's spectral content. This can be done by requiring the selected components to have at least a certain fraction of their spectral density within a preset frequency band. This approach differs from the DFT approach in that not all frequency components outside the desired band are filtered out, but only those that are not in some way related to the desired sources.

For example, Sammali *et al.* [34] determined a band of singular components for ST of uterine motion based on the component's spectral energy within the clinically relevant bandwidth of uterine contractions, and Yu and Lovstakken [25] reported on removing components with a mean Doppler value in a certain clutter frequency band. Alternatively, Wu *et al.* [84] enhanced motion artifacts prior to motion compensation by iteratively determining the weights for every PCA component so that the full-image energy content within a predefined frequency band was maximized with respect to the total.

5) Spatial Coherence: In a similar approach, one could look at the spatial content of each component. As all spatial dimensions are condensed in the Casorati matrix, the spatial image of each component first has to be reconstructed. Subsequently, for example, the spatial frequencies present in each spatial vector reflect the size of the structures that are visualized and could, therefore, be used to select smaller scale structures such as individual bubbles in super-resolution imaging. The 2-D spatial autocorrelation quantified by, e.g., the 2-D full-width half-maximum may represent a more robust measure for spatial coherence; white noise would have the shape of a delta function, whereas highly coherent effects, such as shadowing, might have a very broad profile. Alternatively, [17], [71], [72] looked at the spatial similarity between the different spatial singular vectors. Specific blocks of high spatial similarity were found to be related to clutter, signal, and noise, and the boundaries of the signal block were adaptively estimated.

6) Model Fitting: Finally, one could also only select those components of which the temporal or spatial vectors have expected shapes. For instance, when filtering out the bolus dynamics from a contrast video, only the components that have a bolus-like shape are usable. Analogously, super-resolution components should exhibit sparsity, and for ST in cardiac or uterine movies, a certain degree of periodicity can be assumed. Components with a significantly different behavior are likely to contain clutter or noise. However, it should be noted that, in particular for SVD and PCA, only the combination of certain components might make up a meaningful source signal.

IV. Application of BSS Filtering in Ultrasound Imaging

To evaluate the described adaptive BSS framework, we applied this type of filtering in three different US applications: 1) US localization microscopy; 2) TIC modeling; and 3) US ST. Since, for each application, different source signals are considered desired and undesired, we briefly introduce each application and its dedicated BSS filtering. To compare the results with nonfiltered or conventionally filtered data, we also introduce an objective performance measure for verification both *in silico* and *in vitro*. Finally, we also apply BSS filtering to an *in vivo* example of each application. For reference, the adopted application-specific thresholds are listed in Table II.

A. Ultrasound Localization Microscopy

Super-resolution microvascular imaging by ultrasound localization microscopy (ULM) is a relatively recent development within the field of US, primarily inspired by advances in optical super-resolution [85]. It exploits the known backscattering nature of ultrasound contrast agents (UCAs), which are microbubbles with a size comparable to red blood cells, to track and visualize their position with a higher precision than the resolution of the imaging system [2]. In this way, super-resolved images can be generated, which reveal vascular structures beyond the diffraction limit.

Accurate, uncorrupted detection of isolated UCA signals is vital to this technique. Its fidelity is, therefore, largely affected by noise, clutter, and movement. Even if contrast-specific imaging is used [86], signals arising from tissue are still present. To cope with this problem, SVD-filtering is already widely applied for this purpose, aimed at removing the spatiotemporally highly coherent clutter by omitting a certain number of the lowest order singular components. The number of excluded components can be preset [19], [20], [66] or adaptively determined to optimize tissue–vessel contrast [18], [21]. The reported preset thresholds concerned the 10 and 20 to 30 first components without further clarification [20], [66]; in cases where thresholds were chosen experimentally, the optimal CNR was found by excluding approximately the first 30 components [18], [21]. However, there might still be (higher singular order) components that only carry noise [17], [18], [18], [21]. In that respect, the isolation of the UCA signals is twofold: 1) separation of microbubbles and tissue and 2) removal of electronic and speckle noise.

In our adaptive BSS framework (i.e., where the thresholds are based on components characteristics rather than experiment), we, therefore, assess a combination of component selection methods. First, for the lossless methods only, we remove the noise using information-theoretic criteria, a component energy threshold or noise modeling. Subsequently, for all methods, we examine either the spatiotemporal spectral content, spatial coherence, or sparsity of each component to separate the clutter from the signal. Here, we define $\mathbf{X} \in \mathbb{R}^{N_x \cdot N_y \times N_t}$ as the received RF data, where N_x and N_y are the image sizes in x and y, respectively, and N_t is the number of frames.

As the tissue moves slowly compared with blood and is spatially much more coherent [14], [17], [65], we favor high-frequency and spatially low-coherent components. Component sparsity is quantified by the normalized kurtosis of the spatial vector $\hat{\kappa}_4 = N(\Sigma_{k=1}^{N} Q_k^4) \setminus (\Sigma_{k=1}^{N} Q_k^2)^2$, where Q is the pixel

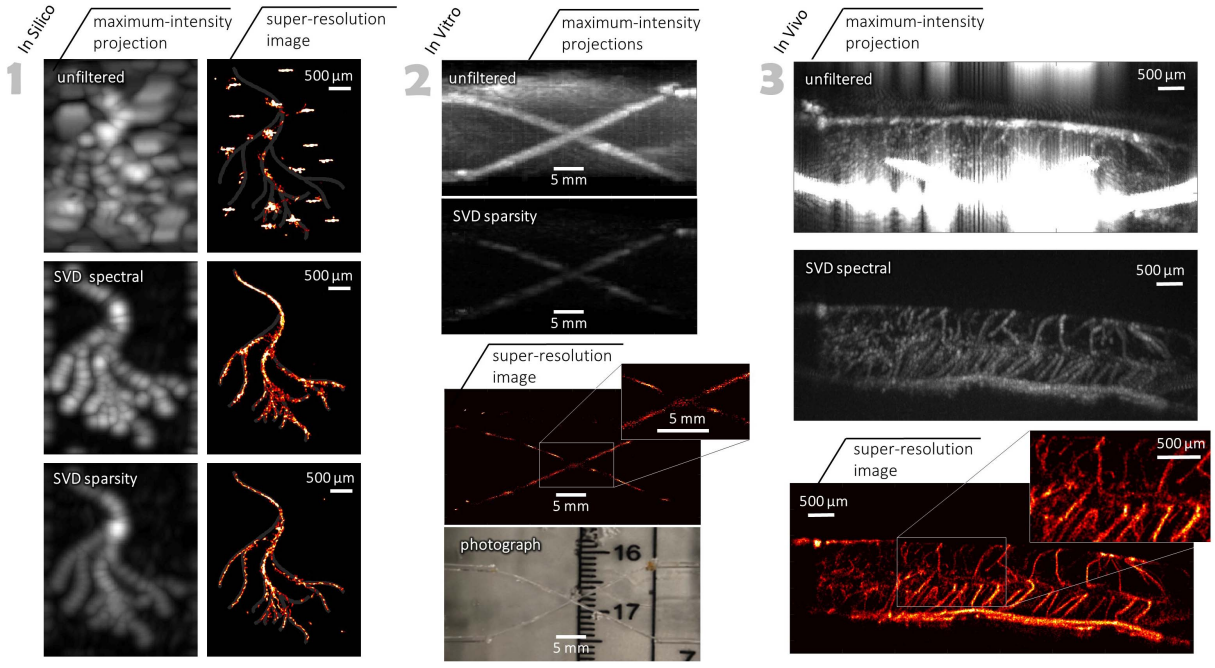

Fig. 2. (1) *In silico* verification of BSS for super-resolution imaging, depicting maximum intensity projections and super-resolution images overlaying the artificial vascular phantom. (2) Super-resolution image of a phantom with two diagonal vessels, compared with a photographic ground truth. (3) Super-resolution image of a rat's spinal vasculature after SVD-spectrally filtered data preprocessing.

gray levels and N is the number of pixels [77]. Table II lists all used cutoff values. As the thresholds for frequency and sparsity depend on image features such as pixel spacing and field of view, we adjust these accordingly for each verification step. Furthermore, we would like to specifically mention that for the "turning points" approach [17], we assess the singular curve and compute the radius of the curvature to find two local minima. As these are assumed to separate the clutter, signal, and noise regimes, the components defined by the values between these minima are assumed to carry the signal.

In this work, we implemented a basic ULM approach. Single UCA centroids were localized in the beamformed image assuming a Gaussian-shaped point spread function (PSF), similar to [1]. BSS was applied to the RF data for all methods except NMF, as the nonnegative nature of backscatter intensity can only be exploited after envelope detection. Subsequently, the super-resolution performance was quantified by the localization F_1-score [87], which, in this case, reads

$$F_1 = \frac{2tl}{2tl + fl + ml} \tag{18}$$

in which, for each pixel, tl accounts for a true, fl for a false, and ml for a missed localization. The F_1-score is hence a reflection of the tradeoff between the wrong and missed localizations.

1) In Silico Verification: To compare the BSS filtering techniques for ULM, a relatively sparse *in silico* phantom was designed to specifically highlight how these algorithms generally cope with intervessel distances below the diffraction limit, clutter domination with multiple clutter scatterers per resolution cell, and clear image deterioration due to ultrasound interference. US imaging of microbubbles traveling through a (micro)vascular network was simulated by propagating 26 microbubbles with random backscatter coefficients along digitally generated trajectories at 2 mm/s (comparable with the fifth-generation microvasculature [88]), in a similar approach as in [19]. Subsequently, we mimicked the tissue signal by adding 500 scatterers of random backscatter intensities that were on average 1/3 lower than that of the microbubbles. These tissue scatterers moved together following a random walk at a speed of approximately 0.2 mm/s. Image formation was then simulated through the 7-MHz-modulated PSF: a 2-D Gaussian with a standard deviation of 0.14 mm and 0.16 mm in the axial and lateral directions, respectively. The simulation resulted in a 2-s CEUS video of size 116×146, with a pixel spacing of 0.03×0.03 mm and a frame rate of 400 Hz.

We found that especially the SVD-based approach in combination with spectral, turning-point, and sparsity-based criteria yielded the best F_1 scores of 0.86, 0.84, and 0.84, respectively. A spectral threshold of $f > 10$ Hz (roughly resembling the PSF traveling at 2 mm/s) and a sparsity threshold of $\hat{\kappa}_4 > 8$ (corresponding roughly to half $\hat{\kappa}_4$ of 13 PSFs in an empty measurement domain) were adopted. For comparison, the nonfiltered and DFT-filtered image yielded the scores of 0.29 and 0.64, respectively. Although the noise threshold did not significantly affect the performance, appropriate thresholds allowed a substantial reduction in the number of components to be included. ICA and NMF had difficulty in representing the sparse source signals but could identify the clutter. Subsequently, subtracting the clutter sources from the original video led to an appreciable F_1-score of 0.86. We refer to Fig. 2(1) for an illustration of the filtering performance and to Table I in the Supplementary Material for the full comparison.

2) In Vitro Verification: We evaluated both spectral and sparsity-based BSS filtering on an *in vitro* phantom consisting of two 300-μm channels crossing each other in a slab of polyacrylamide. The phantom was infused with a 1/500 dilution of ∼1-mL SonoVue UCA (Bracco, Milan, Italy) at 5.9 mm/s. It was imaged for 10 s with a Vantage ultrasound system (Verasonics, Seattle, WA, USA), equipped with a 3.5-MHz L11-4V probe, at a frame rate of 100 Hz, a resolution of 0.5 mm, and a size of 249 × 295 with the pixel spacing of 0.15 × 0.15 mm. Whereas, this phantom is comparable with the *in vivo* situation in terms of scattering by material inhomogeneities and noise levels, it does not include a vessel-like structure or deliberate motion artifacts.

Following the same reasoning as for the *in silico* verification, a frequency and sparsity threshold >12 Hz and >50 were chosen, respectively. In Fig. 2(2), it can be appreciated how the filtering effectively removes the background clutter. Using a photograph of the phantom as a reference, an F_1-score of 0.79, 0.82, and 0.83 was maintained for the spectral, turning-point, and sparsity criteria in the *in vitro* situation. In contrast to the simulations, the choice of noise criterion was more critical to ensure a high super-resolution performance. In particular, the noise modeling strategies (i.e., Marčenko–Pastur) proved useful, the information-theoretic criteria being too strict due to the dominance of clutter. The ICA approach failed to remove the clutter.

3) In Vivo Verification: To assess the performance of the BSS techniques *in vivo*, we filtered a high-frame-rate CEUS acquisition of a rat spinal cord. For this, a Sprague-Dawley rat (Harlan Labs, Indianapolis, IN, USA) was imaged at the University of Washington [89]. The study was approved by the Institutional Animal Care and Use Committee and all appropriate guidelines were followed. The spinal cord was exposed by laminectomy. After tail-vein infusion of 0.15 mL of Definity (Lantheus, N. Billerica, MA, USA), 400-Hz CEUS was performed with the Vantage scanner (Verasonics, Seattle, WA, USA) equipped with a 15-MHz transducer. A power-modulation scheme was adopted for contrast enhancement [90]. The video consists of 720 frames and has a pixel spacing of 0.03 × 0.03 mm; the super-resolved image has a 10-μm pixel spacing.

The spectral and sparsity thresholds were adjusted to $f > 50$ Hz and a sparsity threshold of $\hat{\kappa}_4 > 25$ to fit the *in vivo* acquisition. In absence of a ground truth, we can only qualitatively compare the images [see Fig. 2(3)]. While the sparsity-based and turning-point approaches could not remove all artifacts, the spectral approach was robust for *in vivo* use.

B. Contrast-Ultrasound Time-Intensity Curve Analysis

The intravascular nature of UCAs does not only allow CEUS imaging to visualize vascularity, but it can also be used for quantification of blood flow and perfusion. Over the years, several methods have been developed to extract meaningful features from the evolution of contrast intensity over time, referred to as TICs [91]. For example, extracted parameters were shown to correlate with tumor presence or progression (after treatment) in, e.g., liver, thyroid, breast, kidney, and prostate [92], [93]. In addition, CEUS quantification has been shown useful to estimate, e.g., pulmonary blood volume [94], [95]. Quantification of CEUS can be performed either using a bolus injection [4] or a continuous infusion combined with a disruption-replenishment technique [96].

BSS has been used in dynamic CEUS to eliminate breathing artifacts in parametric abdominal perfusion recordings, using ICA [97] or NMF [98], where the respiratory component was identified based on its frequency content or energy, respectively. In the remainder of this section, we will focus on filtering CEUS videos for lesion localization in the prostate using a bolus injection. However, the implementation can readily be extrapolated to perfusion quantification in other organs. More specifically, BSS was employed to retrieve the TIC wash-in time (WIT), a heuristic parameter often used to assess tissue perfusion [91]. The performance was quantified by both the coefficient of determination (R^2) reflecting the goodness of fit of the TIC by the physics-driven local density random walk (LDRW) model [4], [99] and the relative error in the WIT estimation (ΔWIT) at each pixel. We, therefore, define our data $\mathbf{X} \in \mathbb{R}^{N_x \cdot N_y \times N_t}$ as the beamformed CEUS cine loops. As the influx of UCAs is the dominant signal in these videos, all single-threshold techniques were implemented such that the high-frequency, low-coherence, and noise-containing components are removed.

1) In Silico Verification: The 2-D CEUS imaging of the prostate was simulated using a ∼4 × 4-cm 2-D phantom image containing two lesions. For each pixel (∼0.5 mm, reflecting the resolution of a iU22 commercial scanner (Philips, Bothell, WA, USA) at ∼4 cm [100]), TICs were simulated using the LDRW model and parameters typically encountered in malignant lesions (i.e., $\kappa = 1 \pm 0.1$ s^{-1} and 2 ± 0.1 s^{-1} and $\mu = 25 \pm 1$ s and 15 ± 0.1 s) and benign tissue (i.e., $\kappa = 0.5 \pm 0.1$ s^{-1} and $\mu = 30 \pm 0.1$ s) [99]. The resulting 2-min videos were subsequently degraded by multiplicative noise, a scanner-specific PSF modeled by a Gaussian spatial smoothing filter ($\sigma_x = 1$ mm), a sinusoidal 1-mm motion artifact resembling a breathing frequency of 0.2 Hz [101], random-walk displacement representing manual probe handling, and Gaussian-distributed electronic noise (SNR of ∼4 dB compared with mean signal). Again, based on the iU22 scanner, a frame rate of 10 Hz was adopted.

All BSS methods and component selection criteria were evaluated for this simulation. In general, the relevant TIC dynamics were captured in the first few components of each BSS technique [see Fig. 3(1)]. Although many selection criteria yielded a similar performance, spectral thresholding of PCA and ICA was generally superior in terms of median goodness of fit (both $R^2 > 0.99$) and error in parameter estimation, ΔWIT = 5% and 5.1%, respectively. The unfiltered, 0.15-Hz DFT and 0.5-mm spatially smoothed images yielded the performances of $R^2 = 0.14$, 0.94, and 0.71 and ΔWIT = 12.2%, 12.1%, and 5.5%, respectively. Full results are provided in Table II in the Supplementary Material.

2) In Vitro Verification: In vitro testing comprised a sponge encapsulated in gelatin that was perfused with a bolus of 1-mL SonoVue (Bracco, Milan, Italy) UCA dilution in 10-mL saline and imaged in the contrast mode with the Vantage ultrasound system (Verasonics, Seattle, WA, USA), using a

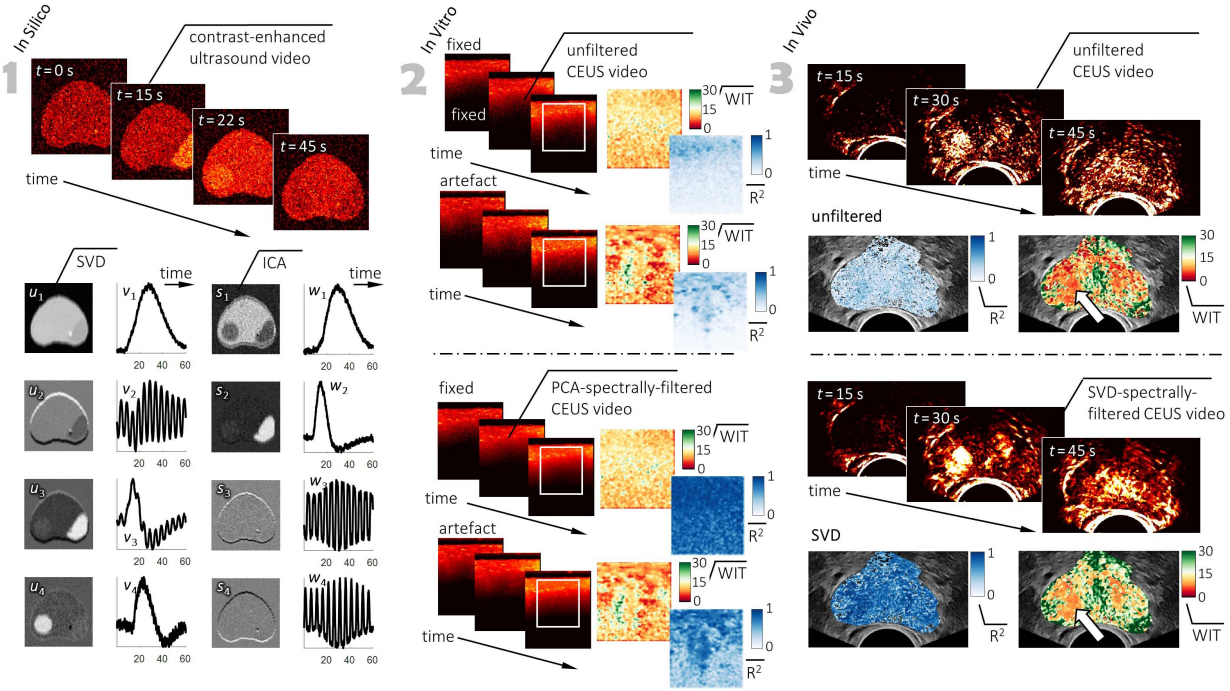

Fig. 3. (1) First four component vectors after SVD and ICA of an *in silico* transrectal CEUS video of the prostate with two, early-enhancing regions. (2) TIC modeling results of the contrast bolus infused into a sponge phantom, with and without a deliberate artifact. (3) Unfiltered and SVD-spectrally filtered *in vivo* CEUS video with the corresponding R^2 and WIT maps; a prostate cancer lesion was found at the location of the arrow.

3.5-MHz L11-4V transducer. The images were ∼2 min long and had at a frame rate of 50 Hz and a pixel spacing of 0.18 × 0.18 mm. Recordings were performed with the probe fixed to the setup, the probe subjected to controlled motion, and the probe undergoing irregular handheld movements. After filtering, the TICs were measured at each pixel, linearized, and fit by the LDRW model. Since the simulations were based on the LDRW model, thus allowing for a perfect fit, nonsynthetic data were expected to yield lower fitting performances due to the limitations of the model. The unfiltered and 0.5-mm spatially smoothed data could be fit with an R^2 of 0.17 and 0.66 in the fixed scenario and 0.14 and 0.44 in the worst-case scenario, respectively. Both spectrally filtered PCA and ICA were able to generate data with R^2-scores of 0.87 and 0.83 in the fixed and 0.54 and 0.62 in the worst-case scenario. The WIT estimates were similar over all methods.

3) In Vivo Verification: In a prospective 48-patient trial at the Martini Klinik (University Hospital, Hamburg-Eppendorf, Germany), patients with biopsy-proven prostate cancer underwent three CEUS recordings with an Aixplorer ultrasound scanner (Supersonic Imagine, Aix-en-Provence, France) equipped with a 3.2-MHz SE12-3 probe at a frame rate of 27 Hz. After radical prostatectomy, prostate histopathology was matched to the CEUS images by assigning benign and malignant regions of interest. By extracting the pixel-wise WIT in those regions, we evaluated this metric's diagnostic potential in terms of the area under the receiver operating characteristics curve (ROC-AUC).

By appending the preprocessing with a spectral-threshold-based SVD and to a lesser extent with PCA, we found an improvement in tumor classification compared with the conventionally filtered recordings, increasing the ROC-AUC from 0.66 to 0.68 for prostate cancer. The goodness of fit (R^2) improved only slightly from 0.68±0.07 to 0.69±0.12, but we observed a substantial decrease in the number of TICs that could not be fit by the LDRW model (from 23% to 14%). As these nonfit pixels are usually left blank when presented to the clinician, filtering clearly allows for a more complete assessment of especially low-quality recordings. Hence, the use of BSS substantially improved the parametric maps while also increasing the classification performance. Fig. 3(3) shows an example of filtered images.

C. Ultrasound ST

US ST imaging allows quantitative evaluation of global and regional tissue motion. A speckle is commonly defined as a typical spatial distribution of grey-level values in US B-mode images caused by constructive and destructive interference of reflections from individual tissue scatterers, forming a unique and deterministic pattern. ST techniques track the speckle pattern during the subsequent frames allowing for motion and strain imaging analysis. ST by US imaging is an active field of research that has already been translated into several applications, in particular, for cardiovascular [102] and muscular [103] investigations and vector Doppler imaging [104]–[106] and, recently, for the assessment of uterine motion outside pregnancy [34]. Motion tracking technology is based on the estimation of tissue displacement rather than on exact formulas; therefore, the presence of small errors is inescapable during the evaluation of relative motion. Errors can occur in the estimated displacements when these inaccuracies accumulate over the consecutive frames.

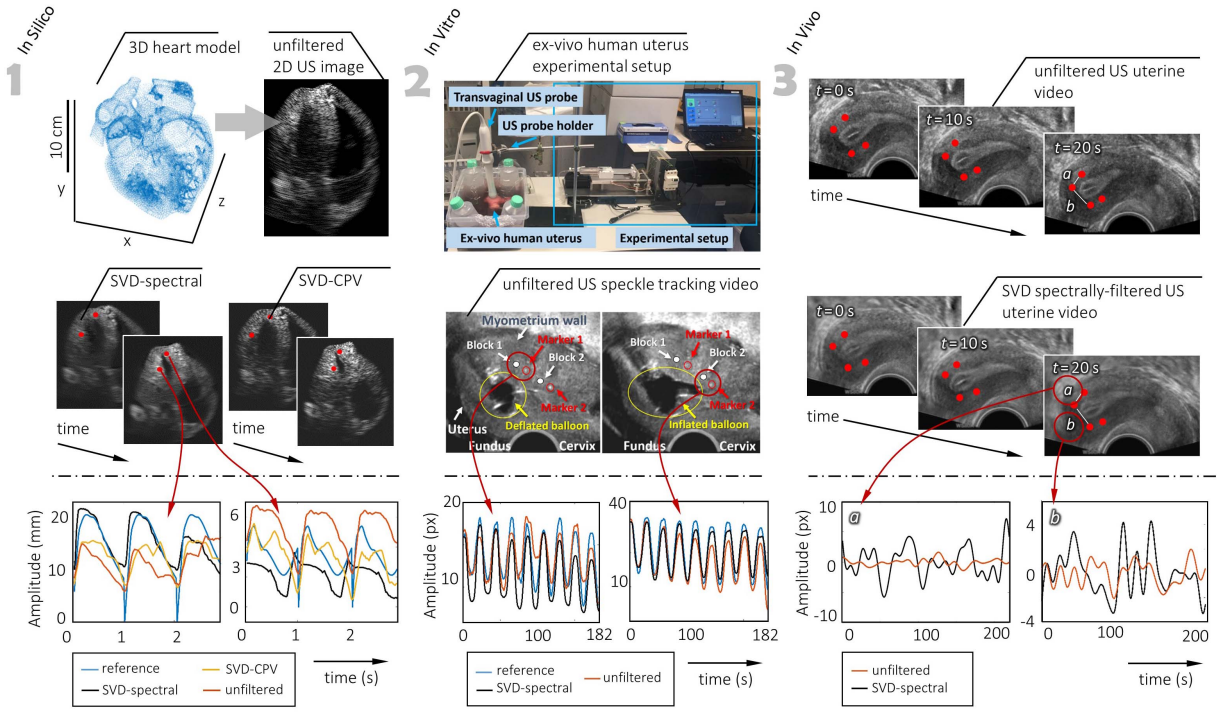

Fig. 4. (1) 3-D finite-element model of a human heart and the corresponding 2-D US simulation that was SVD-spectrally and CPV-filtered prior to ST. (2) Experimental setup inducing controlled, rhythmic motion during 2-D US imaging of an *ex vivo* uterus; the blocks' position during deflation and inflation used for ST are indicated in the unfiltered uterine images. (3) Unfiltered and SVD-spectrally filtered US uterine video used for the comparison of motion tracking along (a) longitudinal and (b) transversal directions.

US loops recorded, e.g., in the heart, skeletal muscle, and uterus comprise slow and fast tissue movement, respiratory motion, stationary tissue clutter, shadowing, and other artifacts. ST algorithm may underestimate the true motion due to the noise and artifacts present in the images, which limits the performance of the ST algorithm. To mitigate the effect of clutter and noise on tracking results, BSS filtering can be performed to suppress the signals that are uncorrelated with tissue motion signals and that affect UST results. BSS has been mostly used for blood velocity estimation [14], [107] as well as for clutter suppression to enhance skeletal muscle displacement [108] using UST where the blood component and the true muscle motion were identified based on its spectral content or energy.

For this work, we studied the effect of BSS filtering prior to US ST in an *in silico* cardiac image sequence, an *ex vivo* uterine motion acquisition, and an *in vivo* uterine recording. The B-mode videos were defined as our data $\mathbf{X} \in \mathbb{R}^{N_x \cdot N_y \times N_t}$. Similar to TIC modeling, the desired signal is generally the most prominent signal in this application, and thus, the first few BSS components were selected for the single-threshold methods. Furthermore, as we apply ST to periodic movements, we adopted periodicity as an additional criterion for component selection. For this criterion, we compute the normalized temporal autocorrelation of each component and only include those with a sufficiently high autocorrelation peak (i.e., >0.6) aside from the one at zero lag.

To objectively assess the tracking quality in terms of agreement with the reference motion before and after BSS filtering, the Pearson correlation coefficient (Pearson r) and mean squared error (mse) were employed as metrics.

1) In Silico Verification: To study the effect of BSS filtering on ST echocardiography, a synthetic 2-D cardiac US acquisition was simulated and tracked over several cardiac cycles. The video was generated using a 3-D finite-element model of the human living heart that follows cardiac excitation and contraction based on a two-field finite-element formulation of coupled electrical and mechanical fields [109]. The finite-element nodes moving with the mechanical deformation of the heart served as US scatterers. A 2-D four-chamber view by a phased-array transducer was created by 3-D modeling 161 scan lines positioned every 0.6° in a coronal plane. For each line, all scatterer contributions were simulated by a convolution between the scatterer location and the location-dependent PSF. This PSF was approximated by assuming a Fraunhofer pressure field modulated by a four-cycle 2.5-MHz cosine function in the propagation direction. In order to reduce the sidelobes of the rectangular transducer, Hamming apodization was adopted [110]. Prior to generating a 54-Hz multicycle US heart video through demodulation of the scan lines, clutter and Gaussian noise were introduced in the RF data. The resulting 1334×1001 2-D US video of the heart had a pixel spacing 0.15 mm and consisted of 432 frames, the first of which is shown in Fig. 4(1).

On the 2-D US synthetic heart image, speckles associated with tissue deformation of the left ventricle (LV) can be identified and tracked by calculating frame-to-frame changes. Out-of-plane motion occurs due to rotation and motion of the

heart into the chest cavity and may cause the disappearance of the speckles over a few frames [111].

In this work, a pyramidal Lucas–Kanade optical flow method was implemented for the tracking, as this method provides sufficient tracking accuracy for large and fast motion [112]. Two blocks were manually selected in the LV wall [see Fig. 4(1)] and tracked over time during three cardiac cycles of the video, both before and after BSS filtering. The estimated motion of the tracked blocks, calculated as the absolute motion (i.e., Euclidean distance from the initial position), was compared with the absolute motion of the corresponding scatterer in the 3-D finite-element model.

All BSS methods and component selection criteria were evaluated for this *in silico* verification [see Fig. 4(1)]. Only four selection criteria yielded an improved performance compared with unfiltered US image sequences. Among these four criteria, the CPV of SVD-filtered data revealed to be generally superior in terms of correlation coefficient (Pearson $r = 0.72\pm0.08$), while [0.5 Hz − 1.5 Hz]-spectral thresholding of the SVD was superior in terms of mse (mse $= 0.0048\pm0.0032$ mm^2). ST on the unfiltered US image sequences yielded performances of Pearson $r = 0.64\pm0.06$ and mse $= 0.13\pm0.1$ mm^2. Table III in the Supplementary Material shows the full results.

2) In Vitro Verification: The use of BSS filtering in ST *in vitro* and *in vivo* is evaluated in US imaging of the uterus. Similar to the heart, uterine US loops not only capture the uterine motion (i.e., uterine peristalsis) but also fast motion of neighboring organs, respiration, and probe motion. First, all BSS methods and component selection criteria were evaluated in an *ex vivo* human uterus, removed by laparoscopic hysterectomy, undergoing controlled and rhythmic motion to establish a reference for the assessment of ST performance. The US acquisitions were performed at Catharina Hospital (Eindhoven, The Netherlands). The patient signed informed consent; all the acquired US postsurgical loops were exempt from relevant ethical committee approval.

The controlled motion was generated by a dedicated experimental setup described in [113]; a sinusoidal displacement of a syringe piston was generated by an electromagnetic actuator injecting saline water through a balloon catheter inserted into the uterine cavity. Rhythmic inflation and deflation of the uterine cavity was generated with a period of 20 s corresponding to a frequency of 0.05 Hz, representing the averages during the most active phase of the menstrual cycle [114]. Reference for the uterine motion was realized by inserting two needles in the myometrial wall.

The 4-min US recording was performed immediately after surgical removal of the uterus with a US scanner WS80A (Samsung Medison, Seoul, South Korea) equipped with a transvaginal V5-9 probe imaging at 5.6-MHz central frequency. The employed frame rate was 30 Hz, amply sufficient to meet the Nyquist condition given the limited bandwidth of the uterine motion [115]. A block-matching ST technique was applied based on 12 blocks that were manually positioned around each needle marker, as described in [113].

In general, the relevant uterine dynamics were captured in the first few components of each BSS technique. Many selection criteria yielded comparable ST performances in terms of Pearson r between the average of the 12 blocks and the needle marker, but spectral thresholding of SVD performed best both in Pearson r (0.84 ± 0.15) and mse (0.29 ± 0.24 mm^2), outperforming ST of the unfiltered data (Pearson $r = 0.66\pm0.38$ and mse $= 0.34\pm0.30$ mm^2). As uterine dynamics are slower than the heart contractions, a frequency interval $f_c = [0.04$ Hz − 0.06 Hz] was used.

3) In Vivo Verification: For the ethical-committee-approved study described in [34], several healthy women underwent 4-min US recordings during four selected phases of the natural menstrual cycle, suggested to indicate variations in uterine contractility [116]. The US scanner and settings were the same as in the *in vitro* acquisitions, and four blocks were manually defined along the myometrial wall in the fundus area, which is considered to be the most contractile part of the uterus. These four sites were then tracked over time by a dedicated US ST algorithm [34] and the Euclidean distances between the longitudinal and transversal pairs, as shown in Fig. 4(3), served as a measure of absolute motion.

For this work, we evaluated the spectral thresholding of SVD by adjusting the frequency interval to $f_c = [0.008$ Hz − 0.066 Hz] to cover the entire motion range of the different menstrual cycle phases. We extracted the median frequency (MF) from both filtered and unfiltered distance signals as representative of uterine motion frequency for the given example in Fig. 4(3). The filtered signal presented MF = 0.0360 Hz, while the unfiltered signal yielded MF = 0.0176 Hz, indicating that the BBS filtering produces better estimates of the contraction frequency when the values reported in the literature for the specific menstrual phase are considered as ground truth (0.035–0.055 Hz [115]). Indeed, as can be appreciated in Fig. 4(3), larger uterine motions can be tracked, which may lead to a more robust estimate of the MF.

V. Discussion

In this work, we reviewed and compared several BSS approaches for noise and clutter suppression in US recordings. As the nature of the desired signal differs among applications, it is important to tailor a filtering approach to the acquisition at hand using specific domain knowledge. Furthermore, although the decompositions comprising BSS are intrinsically adaptive, the retrieval of the signal subspace is often performed manually. Adaptive strategies to identify the components that make up the desired signal are far from established; therefore, we also focused on several adaptive criteria for component (i.e., "source") rejection. After all, even though it is possible that the qualitatively best-looking images are formed using a heuristic or empirical rather than an adaptive approach, especially when optimizing CNR, such a strategy has limited generalizability and reproducibility. Clutter source dominance as well as noise levels can substantially change from acquisition to acquisition. While Demené *et al.* [14] observed that the cutoff value is not critical, we have found substantial differences in the applications investigated. A similar experience is reported in [17].

For the discussed applications, well-tailored BSS filtering outperformed the more traditional filtering techniques.

Probably, the reason for this is that BSS exploits the statistical independence or orthogonality of the image "sources"; therefore, it is less affected by the overlap of clutter and noise in the spatial or temporal (frequency) domain. Although we aimed to design our simulations in such a way that they represented typical filtering challenges for our systematic comparison, it has not been possible to cover all subtle differences among the US data and methods. Some caution should, therefore, be exercised in the interpretation of the results.

Nevertheless, we found that for all US applications considered in this work, SVD in combination with spectral thresholding generally performed among the best. This technique exploits the known temporal characteristics of the desired sources aside the BSS decomposition; nonnoise high-frequency components revealed UCA signals in ULM, the low-frequency components harbored the TIC information, and a well-chosen frequency passband allowed for the separation of cardiac and uterine motion from uncorrelated sources and noise contamination in US ST. Of all BSS techniques examined, SVD best isolated the temporal components for this purpose.

On the other hand, while ICA and NMF show benefit for TIC modeling, they underperform for super-resolution. This is the result of the linear mixing matrix assuming a steady state, as a consequence of which spatial translation over time cannot be captured by a limited number of components. We believe that for blood flow imaging, where clutter is abundant but blood vessel signals are less sparse, also ICA and NMF could be considered. Also in US ST, NMF underperformed compared with the other BSS methods, possibly because periodic motion is best approximated by allowing negative values. This effect can be appreciated within the first few components of the *in silico* TIC modeling validation, where the simulated breathing frequency is clearly visible.

It is worth noting that BSS techniques, which decompose based on spatiotemporal coherence, are limited in coping with noise sources that have low temporal and spatial coherence due to, e.g., motion [117]. In Fig. 3(1), the effect of temporally coherent motion can be recognized in the second component of SVD and both the third and fourth components of ICA. As its temporal characteristics are in this case different from the signal dynamics, these effects can be filtered out. To correct for movements with low spatial/temporal coherence, which are not easily identified in specific BSS components, other techniques, such as (elastic) registration or coherent flow power Doppler [117], are required.

Another drawback of BSS techniques is that they generally require substantially more computational power and time compared with conventional filters, in particular when dealing with the vast amount of data obtained in ultrafast imaging and long-running acquisitions. As all spatial dimensions are collected as rows in the Casorati matrix, filtering can easily be extended to volumetric videos. In fact, as discussed in [14], the availability of a larger spatial support might even lead to an improved BSS performance.

Although beyond the scope of this article, there are methods available to speed up processing without compromising the accuracy or effectiveness of the decomposition itself, for example, randomized SVD [64] or a block-wise method as proposed in [18]. The latter method even allows for a more accurate clutter and noise rejection, as it can adapt to spatial variations in SNR and resolution. Alternatively, one could think of an approach in which frequency requirements are adjusted during the recording, for example, having a different frequency threshold for different phases of the cardiac cycle [14]. In one such approach [69], the ideal clutter cutoff was manually initialized for the first 60 frames and then adaptively retained by tracking the evolution of singular values for each consecutive 60-frame SVD as the coronary ultrafast Doppler video progressed.

Even more promising are approaches that circumvent filter cutoff values by integrating filtering in the BSS algorithm. A straightforward example is the RPCA approach introduced in Section II; for the simulation of ULM in which the signal is sparse, an F_1-score of 0.92 was reached. Separation of sparse and low-rank matrices is also studied for sparse signal separation [118]–[120]. Also, deep learning could be utilized to speed up the recovery of sparse sources [19].

It remains to be investigated, whether a gradual rather than a hard threshold can improve BSS filtering by avoiding block artifacts, as mentioned in [16]. Furthermore, although most authors use a cutoff value and some observe artifacts caused by partial removal of a complementary subset of components [34], the inclusion of only consecutive singular components is not strictly required. As shown in Fig. 3(1), a single component could represent an artifact, whereas the surrounding components carry the desired signal. This is, however, dependent on the application and should be studied in more detail.

VI. Conclusion

BSS filtering is increasingly applied to US acquisitions and exhibits great potential for effective noise and clutter suppression. However, as BSS as well as subspace selection has to be tailored to an application, the choice and dedicated design of such a filter are of vital importance. Here, we have determined the best domain knowledge-based adaptive approaches for BSS filtering in several US applications.

References

[1] C. Errico *et al.*, "Ultrafast ultrasound localization microscopy for deep super-resolution vascular imaging," *Nature*, vol. 527, no. 7579, pp. 499–502, Nov. 2015.

[2] O. Couture, V. Hingot, B. Heiles, P. Muleki-Seya, and M. Tanter, "Ultrasound localization microscopy and super-resolution: A state of the art," *IEEE Trans. Ultrason., Ferroelectr., Freq. Control*, vol. 65, no. 8, pp. 1304–1320, Aug. 2018.

[3] P. A. Heidenreich *et al.*, "*In vitro* calculation of flow by use of contrast ultrasonography," *J. Amer. Soc. Echocardiography*, vol. 6, no. 1, pp. 51–61, Jan. 1993.

[4] C. Strouthos, M. Lampaskis, V. Sboros, A. Mcneilly, and M. Averkiou, "Indicator dilution models for the quantification of microvascular blood flow with bolus administration of ultrasound contrast agents," *IEEE Trans. Ultrason., Ferroelectr., Freq. Control*, vol. 57, no. 6, pp. 1296–1310, Jun. 2010.

[5] R. Jasaityte, B. Heyde, and J. D'hooge, "Current state of three-dimensional myocardial strain estimation using echocardiography," *J. Amer. Soc. Echocardiography*, vol. 26, no. 1, pp. 15–28, Jan. 2013.

[6] P. Collier, D. Phelan, and A. Klein, "A test in context: Myocardial strain measured by speckle-tracking echocardiography," *J. Amer. College Cardiol.*, vol. 69, no. 8, pp. 1043–1056, Feb. 2017.

[7] S. Bjaerum, H. Torp, and K. Kristoffersen, "Clutter filter design for ultrasound color flow imaging," *IEEE Trans. Ultrason., Ferroelectr., Freq. Control*, vol. 49, no. 2, pp. 204–216, Feb. 2002.

[8] T. Joel and R. Sivakumar, "An extensive review on despeckling of medical ultrasound images using various transformation techniques," *Appl. Acoust.*, vol. 138, pp. 18–27, Sep. 2018.

[9] P. B. Calóope, F. N. S. Medeiros, R. C. P. Marques, and R. C. S. Costa, "A comparison of filters for ultrasound images," in *Telecommunications and Networking—ICT 2004* (Lecture Notes in Computer Science), vol. 3124, J. N. de Souza, P. Dini, and P. Lorenz, Eds. Berlin, Germany: Springer, 2004.

[10] A. Needles, D. E. Goertz, A. M. Cheung, and F. S. Foster, "Interframe clutter filtering for high frequency flow imaging," *Ultrasound Med. Biol.*, vol. 33, no. 4, pp. 591–600, Apr. 2007.

[11] Y. M. Yoo and Y. Kim, "New adaptive clutter rejection for ultrasound color Doppler imaging: *In vivo* study," *Ultrasound Med. Biol.*, vol. 36, no. 3, pp. 480–487, Mar. 2010.

[12] N. Feng, J. Zhang, and W. Wang, "An adaptive clutter rejection method based on AR model in color flow imaging," *Ultrasonics*, vol. 44, pp. e85–e88, Dec. 2006.

[13] N. Karaboga and F. Latifoglu, "Elimination of noise on transcranial Doppler signal using IIR filters designed with artificial bee colony—ABC-algorithm," *Digit. Signal Process.*, vol. 23, no. 3, pp. 1051–1058, May 2013.

[14] C. Demene *et al.*, "Spatiotemporal clutter filtering of ultrafast ultrasound data highly increases Doppler and fUltrasound sensitivity," *IEEE Trans. Med. Imag.*, vol. 34, no. 11, pp. 2271–2285, Nov. 2015.

[15] C. M. Gallippi, K. R. Nightingale, and G. E. Trahey, "BSS-based filtering of physiological and ARFI-induced tissue and blood motion," *Ultrasound Med. Biol.*, vol. 29, no. 11, pp. 1583–1592, Nov. 2003.

[16] F. W. Mauldin, D. Lin, and J. A. Hossack, "The singular value filter: A general filter design strategy for PCA-based signal separation in medical ultrasound imaging," *IEEE Trans. Med. Imag.*, vol. 30, no. 11, pp. 1951–1964, Nov. 2011.

[17] J. Baranger, B. Arnal, F. Perren, O. Baud, M. Tanter, and C. Demene, "Adaptive spatiotemporal SVD clutter filtering for ultrafast Doppler imaging using similarity of spatial singular vectors," *IEEE Trans. Med. Imag.*, vol. 37, no. 7, pp. 1574–1586, Jul. 2018.

[18] P. Song, A. Manduca, J. D. Trzasko, and S. Chen, "Ultrasound small vessel imaging with block-wise adaptive local clutter filtering," *IEEE Trans. Med. Imag.*, vol. 36, no. 1, pp. 251–262, Jan. 2017.

[19] R. J. G. van Sloun *et al.*, "Super-resolution ultrasound localization microscopy through deep learning," 2018, *arXiv:1804.07661*. [Online]. Available: http://arxiv.org/abs/1804.07661

[20] F. Lin, J. K. Tsuruta, J. D. Rojas, and P. A. Dayton, "Optimizing sensitivity of ultrasound contrast-enhanced super-resolution imaging by tailoring size distribution of microbubble contrast agent," *Ultrasound Med. Biol.*, vol. 43, no. 10, pp. 2488–2493, Oct. 2017.

[21] D. Ghosh, F. Xiong, S. R. Sirsi, P. W. Shaul, R. F. Mattrey, and K. Hoyt, "Toward optimization of *in vivo* super-resolution ultrasound imaging using size-selected microbubble contrast agents," *Med. Phys.*, vol. 44, no. 12, pp. 6304–6313, Oct. 2017.

[22] B. Breyer, T. Viculin, and B. Vojnović, "Noise in ultrasonic imaging," *Ultrasonics*, vol. 18, no. 2, pp. 81–84, Mar. 1980.

[23] C. M. Gallippi and G. E. Trahey, "Adaptive clutter filtering via blind source separation for two-dimensional ultrasonic blood velocity measurement," *Ultrason. Imag.*, vol. 24, no. 4, pp. 193–214, Oct. 2002.

[24] J. L. Mateo and A. Fernández-Caballero, "Finding out general tendencies in speckle noise reduction in ultrasound images," *Expert Syst. Appl.*, vol. 36, no. 4, pp. 7786–7797, May 2009.

[25] A. Yu and L. Lovstakken, "Eigen-based clutter filter design for ultrasound color flow imaging: A review," *IEEE Trans. Ultrason., Ferroelectr., Freq. Control*, vol. 57, no. 5, pp. 1096–1111, May 2010.

[26] J.-F. Cardoso, "Blind signal separation: Statistical principles," *Proc. IEEE*, vol. 86, no. 10, pp. 2009–2025, Oct. 1998.

[27] K. R. Rao and P. C. Yip, *The Transform and Data Compression Handbook*. Boca Raton, FL, USA: CRC Press, 2000.

[28] T. K. Moon and W. C. Stirling, *Mathematical Methods and Algorithms for Signal Processing*. New York, NY, USA: Prentice-Hall, 2000.

[29] G. H. Golub and C. Reinsch, "Singular value decomposition and least squares solutions," *Numerische Math.*, vol. 14, no. 5, pp. 403–420, 1970.

[30] C. Eckart and G. Young, "The approximation of one matrix by another of lower rank," *Psychometrika*, vol. 1, no. 3, pp. 211–218, Sep. 1936.

[31] C. D. Martin and M. A. Porter, "The extraordinary SVD," *Amer. Math. Monthly*, vol. 119, no. 10, pp. 838–851, 2012.

[32] J. Dongarra *et al.*, "The singular value decomposition: Anatomy of optimizing an algorithm for extreme scale," *SIAM Rev.*, vol. 60, no. 4, pp. 808–865, Jan. 2018.

[33] G. W. Stewart, "On the early history of the singular value decomposition," *SIAM Rev.*, vol. 35, no. 4, pp. 551–566, Dec. 1993.

[34] F. Sammali *et al.*, "Dedicated ultrasound speckle tracking for quantitative analysis of uterine motion outside pregnancy," *IEEE Trans. Ultrason., Ferroelectr., Freq. Control*, vol. 66, no. 3, pp. 581–590, Mar. 2019.

[35] A. A. Miranda, Y.-A. Le Borgne, and G. Bontempi, "New routes from minimal approximation error to principal components," *Neural Process. Lett.*, vol. 27, no. 3, pp. 197–207, Jan. 2008.

[36] J. J. Gerbrands, "On the relationships between SVD, KLT and PCA," *Pattern Recognit.*, vol. 14, nos. 1–6, pp. 375–381, Jan. 1981.

[37] P. Duhamel and M. Vetterli, "Fast Fourier transforms: A tutorial review and a state of the art," *Signal Process.*, vol. 19, no. 4, pp. 259–299, Apr. 1990.

[38] N. Kishore Kumar and J. Schneider, "Literature survey on low rank approximation of matrices," *Linear Multilinear Algebra*, vol. 65, no. 11, pp. 2212–2244, 2017.

[39] A. K. Kattepur and F. Sattar, "FebICA: Feedback independent component analysis for complex domain source separation of communication signals," in *Blind Source Separation* (Signals and Communication Technology), G. Naik and W. Wang, Eds. Berlin, Germany: Springer, 2014.

[40] S. Arora, R. Ge, R. Kannan, and A. Moitra, "Computing a nonnegative matrix factorization–provably," *SIAM J. Comput.*, vol. 45, no. 4, pp. 1582–1611, Jan. 2016.

[41] E. J. Candès, X. Li, Y. Ma, and J. Wright, "Robust principal component analysis?" *J. ACM*, vol. 58, no. 3, p. 11, May 2011.

[42] R. Otazo, E. Candès, and D. K. Sodickson, "Low-rank plus sparse matrix decomposition for accelerated dynamic MRI with separation of background and dynamic components," *Magn. Reson. Med.*, vol. 73, no. 3, pp. 1125–1136, Apr. 2014.

[43] T. Bouwmans, S. Javed, H. Zhang, Z. Lin, and R. Otazo, "On the applications of robust PCA in image and video processing," *Proc. IEEE*, vol. 106, no. 8, pp. 1427–1457, Aug. 2018.

[44] C. Lu, J. Feng, Y. Chen, W. Liu, Z. Lin, and S. Yan, "Tensor robust principal component analysis: Exact recovery of corrupted low-rank tensors via convex optimization," in *Proc. Adv. Neural Inf. Process. Syst.*, 2009, pp. 2080–2088.

[45] M. Bayat and M. Fatemi, "Concurrent clutter and noise suppression via low rank plus sparse optimization for non-contrast ultrasound flow Doppler processing in microvasculature," in *Proc. IEEE Int. Conf. Acoust., Speech Signal Process. (ICASSP)*, Apr. 2018, pp. 1080–1084.

[46] O. Solomon *et al.*, "Deep unfolded robust PCA with application to clutter suppression in ultrasound," 2018, *arXiv:1811.08252*. [Online]. Available: http://arxiv.org/abs/1811.08252

[47] G. Chau, Y. L. Li, M. Jakovljevic, J. Dahl, and P. Rodriguez, "Wall clutter removal in Doppler ultrasound using principal component pursuit," in *Proc. IEEE Int. Ultrason. Symp. (IUS)*, Oct. 2018, pp. 1–4.

[48] P. Comon, "Independent component analysis, a new concept?" *Signal Process.*, vol. 36, no. 3, pp. 287–314, Apr. 1994.

[49] A. Hyvärinen and E. Oja, "Independent component analysis: Algorithms and applications," *Neural Netw.*, vol. 13, nos. 4–5, pp. 411–430, Jun. 2000.

[50] S.-I. Amari, A. Cichocki, and H. H. Yang, "A new learning algorithm for blind signal separation," in *Proc. Adv. Neural Inf. Process. Syst.*, 1996, pp. 757–763.

[51] A. J. Bell and T. J. Sejnowski, "The 'independent components' of natural scenes are edge filters," *Vis. Res.*, vol. 37, no. 23, pp. 3327–3338, Dec. 1997.

[52] P. Bai, H. Shen, X. Huang, and Y. Truong, "A supervised singular value decomposition for independent component analysis of fMRI," *Statistica Sinica*, vol. 18, no. 4, pp. 1233–1252, 2008.

[53] D. Jouan-Rimbaud Bouveresse, A. Moya-González, F. Ammari, and D. N. Rutledge, "Two novel methods for the determination of the number of components in independent components analysis models," *Chemometric Intell. Lab. Syst.*, vol. 112, pp. 24–32, Mar. 2012.

[54] Y.-O. Li, T. Adalı, and V. D. Calhoun, "Estimating the number of independent components for functional magnetic resonance imaging data," *Hum. Brain Mapping*, vol. 28, no. 11, pp. 1251–1266, 2007.

[55] A. Hyvarinen, "Fast and robust fixed-point algorithms for independent component analysis," *IEEE Trans. Neural Netw.*, vol. 10, no. 3, pp. 626–634, May 1999.

[56] D. N. Rutledge and D. Jouan-Rimbaud Bouveresse, "Independent components analysis with the JADE algorithm," *TrAC Trends Anal. Chem.*, vol. 50, pp. 22–32, Oct. 2013.

[57] J. F. Cardoso and A. Souloumiac, "Blind beamforming for non-Gaussian signals," *IEE Proc. F-Radar Signal Process.*, vol. 140, no. 6, pp. 362–370, 1993.

[58] A. J. Bell and T. J. Sejnowski, "An information-maximization approach to blind separation and blind deconvolution," *Neural Comput.*, vol. 7, no. 6, pp. 1129–1159, Nov. 1995.

[59] J. V. Stone, "Independent component analysis: An introduction," *Trends Cogn. Sci.*, vol. 6, no. 2, pp. 59–64, 2002.

[60] T.-W. Lee, M. Girolami, and T. J. Sejnowski, "Independent component analysis using an extended infomax algorithm for mixed subgaussian and supergaussian sources," *Neural Comput.*, vol. 11, no. 2, pp. 417–441, Feb. 1999.

[61] D. D. Lee and H. S. Seung, "Learning the parts of objects by non-negative matrix factorization," *Nature*, vol. 401, no. 6755, pp. 788–791, Oct. 1999.

[62] M. W. Berry, M. Browne, A. N. Langville, V. P. Pauca, and R. J. Plemmons, "Algorithms and applications for approximate non-negative matrix factorization," *Comput. Statist. Data Anal.*, vol. 52, no. 1, pp. 155–173, Sep. 2007.

[63] Y.-X. Wang and Y.-J. Zhang, "Nonnegative matrix factorization: A comprehensive review," *IEEE Trans. Knowl. Data Eng.*, vol. 25, no. 6, pp. 1336–1353, Jun. 2013.

[64] P. Song *et al.*, "Accelerated singular value-based ultrasound blood flow clutter filtering with randomized singular value decomposition and randomized spatial downsampling," *IEEE Trans. Ultrason., Ferroelectr., Freq. Control*, vol. 64, no. 4, pp. 706–716, Apr. 2017.

[65] Y. Desailly, A.-M. Tissier, J.-M. Correas, F. Wintzenrieth, M. Tanter, and O. Couture, "Contrast enhanced ultrasound by real-time spatiotemporal filtering of ultrafast images," *Phys. Med. Biol.*, vol. 62, no. 1, pp. 31–42, Dec. 2016.

[66] R. J. G. van Sloun, O. Solomon, Y. C. Eldar, H. Wijkstra, and M. Mischi, "Sparsity-driven super-resolution in clinical contrast-enhanced ultrasound," in *Proc. IEEE Int. Ultrason. Symp. (IUS)*, Sep. 2017, pp. 1–4.

[67] M. A. Lediju, M. J. Pihl, S. J. Hsu, J. J. Dahl, C. M. Gallippi, and G. E. Trahey, "A motion-based approach to abdominal clutter reduction," *IEEE Trans. Ultrason., Ferroelectr., Freq. Control*, vol. 56, no. 11, pp. 2437–2449, Nov. 2009.

[68] M. van der Ven, J. J. Luime, L. L. van der Velden, J. G. Bosch, J. M. W. Hazes, and H. J. Vos, "High-frame-rate power Doppler ultrasound is more sensitive than conventional power Doppler in detecting rheumatic vascularisation," *Ultrasound Med. Biol.*, vol. 43, no. 9, pp. 1868–1879, Sep. 2017.

[69] D. Maresca, M. Correia, M. Tanter, B. Ghaleh, and M. Pernot, "Adaptive spatiotemporal filtering for coronary ultrafast Doppler angiography," *IEEE Trans. Ultrason., Ferroelectr., Freq. Control*, vol. 65, no. 11, pp. 2201–2204, Nov. 2018.

[70] S. Valle, W. Li, and S. J. Qin, "Selection of the number of principal components: The variance of the reconstruction error criterion with a comparison to other Methods," *Ind. Eng. Chem. Res.*, vol. 38, no. 11, pp. 4389–4401, Nov. 1999.

[71] H. Ikeda *et al.*, "Singular value decomposition of received ultrasound signal to separate tissue, blood flow, and cavitation signals," *Jpn. J. Appl. Phys.*, vol. 57, no. 7S1, May 2018, Art. no. 07LF04.

[72] B. Arnal, J. Baranger, C. Demene, M. Tanter, and M. Pernot, "*In vivo* real-time cavitation imaging in moving organs," *Phys. Med. Biol.*, vol. 62, no. 3, pp. 843–857, Jan. 2017.

[73] D. E. Kruse and K. W. Ferrara, "A new high resolution color flow system using an eigendecomposition-based adaptive filter for clutter rejection," *IEEE Trans. Ultrason., Ferroelectr., Freq. Control*, vol. 49, no. 10, pp. 1384–1399, Oct. 2002.

[74] M. Kim, C. K. Abbey, J. Hedhli, L. W. Dobrucki, and M. F. Insana, "Expanding acquisition and clutter filter dimensions for improved perfusion sensitivity," *IEEE Trans. Ultrason., Ferroelectr., Freq. Control*, vol. 64, no. 10, pp. 1429–1438, Oct. 2017.

[75] S. G. Schalk *et al.*, "4-D spatiotemporal analysis of ultrasound contrast agent dispersion for prostate cancer localization: A feasibility study," *IEEE Trans. Ultrason., Ferroelectr., Freq. Control*, vol. 62, no. 5, pp. 839–851, May 2015.

[76] M. Mischi, M. P. J. Kuenen, and H. Wijkstra, "Angiogenesis imaging by spatiotemporal analysis of ultrasound contrast agent dispersion kinetics," *IEEE Trans. Ultrason., Ferroelectr., Freq. Control*, vol. 59, no. 4, pp. 621–629, Apr. 2012.

[77] N. Hurley and S. Rickard, "Comparing measures of sparsity," *IEEE Trans. Inf. Theory*, vol. 55, no. 10, pp. 4723–4741, Oct. 2009.

[78] J. Rissanen, "Modeling by shortest data description," *Automatica*, vol. 14, no. 5, pp. 465–471, Sep. 1978.

[79] H. Akaike, "A new look at the statistical model identification," *IEEE Trans. Autom. Control*, vol. AC-19, no. 6, pp. 716–723, Dec. 1974.

[80] M. Wax and T. Kailath, "Detection of signals by information theoretic criteria," *IEEE Trans. Acoust., Speech, Signal Process.*, vol. 33, no. 2, pp. 387–392, Apr. 1985.

[81] R. J. van Sloun, L. Demi, A. W. Postema, J. J. de la Rosette, H. Wijkstra, and M. Mischi, "Ultrasound-contrast-agent dispersion and velocity imaging for prostate cancer localization," *Med. Image Anal.*, vol. 35, pp. 610–619, Jan. 2017.

[82] V. A. Marčenko and L. A. Pastur, "Distribution of eigenvalues for some sets of random matrices," *Math. USSR-Sbornik*, vol. 1, no. 4, pp. 457–483, Oct. 2007.

[83] C. E. Shannon, "A mathematical theory of communication," *Bell Syst. Tech. J.*, vol. 27, no. 3, pp. 379–423, Jul./Oct. 1948.

[84] K. Wu, X. Zhang, G. Chen, F. Weng, and M. Ding, "Respiratory motion compensation algorithm of ultrasound hepatic perfusion data acquired in free-breathing," *Proc. SPIE*, vol. 8920, Oct. 2013, Art. no. 89200I.

[85] E. Betzig *et al.*, "Imaging intracellular fluorescent proteins at nanometer resolution," *Science*, vol. 313, no. 5793, pp. 1642–1645, Sep. 2006.

[86] O. M. Viessmann, R. J. Eckersley, K. Christensen-Jeffries, M. X. Tang, and C. Dunsby, "Acoustic super-resolution with ultrasound and microbubbles," *Phys. Med. Biol.*, vol. 58, no. 18, pp. 6447–6458, Sep. 2013.

[87] C. Goutte and E. Gaussier, "A probabilistic interpretation of precision, recall and F-score, with implication for evaluation," in *Advances in Information Retrieval*, D. E. Losada and J. M. Fernández-Luna, Eds. Berlin, Germany: Springer, 2005, pp. 345–359.

[88] A. R. Pries, T. W. Secomb, P. Gaehtgens, and J. F. Gross, "Blood flow in microvascular networks. Experiments and simulation," *Circulat. Res.*, vol. 67, no. 4, pp. 826–834, 1990.

[89] Z. Z. Khaing *et al.*, "Contrast-enhanced ultrasound to visualize hemodynamic changes after rodent spinal cord injury," *J. Neurosurg, Spine*, vol. 29, no. 3, pp. 306–313, Sep. 2018.

[90] C. Tremblay-Darveau, R. Williams, L. Milot, M. Bruce, and P. N. Burns, "Combined perfusion and Doppler imaging using plane-wave nonlinear detection and microbubble contrast agents," *IEEE Trans. Ultrason., Ferroelectr., Freq. Control*, vol. 61, no. 12, pp. 1988–2000, 2014.

[91] C. Dietrich, M. Averkiou, J.-M. Correas, N. Lassau, E. Leen, and F. Piscaglia, "An EFSUMB introduction into dynamic contrast-enhanced ultrasound (DCE-US) for quantification of tumour perfusion," *Ultraschall der Medizin-Eur. . Ultrasound*, vol. 33, no. 4, pp. 344–351, Jul. 2012.

[92] M. Claudon *et al.*, "Guidelines and good clinical practice recommendations for contrast enhanced ultrasound (CEUS) in the liver—Update 2012: A WFUMB-EFSUMB initiative in cooperation with representatives of AFSUMB, AIUM, ASUM, FLAUS and ICUS," *Ultrasound Med. Biol.*, vol. 39, no. 2, pp. 187–210, 2013.

[93] E. Fröhlich, R. Muller, X.-W. Cui, D. Schreiber-Dietrich, and C. F. Dietrich, "Dynamic contrast-enhanced ultrasound for quantification of tissue perfusion," *J. Ultrasound Med.*, vol. 34, no. 2, pp. 179–196, Feb. 2015.

[94] I. H. F. Herold, M. A. Soliman Hamad, H. C. van Assen, R. A. Bouwman, H. H. M. Korsten, and M. Mischi, "Pulmonary blood volume measured by contrast enhanced ultrasound: A comparison with transpulmonary thermodilution," *Brit. J. Anaesthesia*, vol. 115, no. 1, pp. 53–60, Jul. 2015.

[95] M. Mischi, T. A. Kalker, and E. H. Korsten, "Contrast echocardiography for pulmonary blood volume quantification," *IEEE Trans. Ultrason., Ferroelectr. Freq. Control*, vol. 51, no. 9, pp. 1137–1147, Sep. 2004.

[96] E. Quaia, "Assessment of tissue perfusion by contrast-enhanced ultrasound," *Eur. Radiol.*, vol. 21, no. 3, pp. 604–615, Oct. 2010.

[97] G. Renault, F. Tranquart, V. Perlbarg, A. Bleuzen, A. Herment, and F. Frouin, "A posteriorirespiratory gating in contrast ultrasound for assessment of hepatic perfusion," *Phys. Med. Biol.*, vol. 50, no. 19, pp. 4465–4480, Sep. 2005.

[98] D. Wang, M. Xiao, Y. Zhang, and M. Wan, "Abdominal parametric perfusion imaging with respiratory motion-compensation based on contrast-enhanced ultrasound: *In-vivo* validation," *Comput. Med. Imag. Graph.*, vol. 65, pp. 11–21, Apr. 2018.

[99] M. P. J. Kuenen, M. Mischi, and H. Wijkstra, "Contrast-ultrasound diffusion imaging for localization of prostate cancer," *IEEE Trans. Med. Imag.*, vol. 30, no. 8, pp. 1493–1502, Aug. 2011.

[100] M. P. J. Kuenen, T. A. Saidov, H. Wijkstra, and M. Mischi, "Contrast-ultrasound dispersion imaging for prostate cancer localization by improved spatiotemporal similarity analysis," *Ultrasound Med. Biol.*, vol. 39, no. 9, pp. 1631–1641, Sep. 2013.

[101] J. Dinkel *et al.*, "Respiratory-induced prostate motion," *Strahlentherapie Und Onkologie*, vol. 187, no. 7, pp. 426–432, Jun. 2011.

[102] R. G. P. Lopata *et al.*, "Cardiac biplane strain imaging: Initial *in vivo* experience," *Phys. Med. Biol.*, vol. 55, no. 4, pp. 963–979, Jan. 2010.

[103] T. Kawagishi, "Speckle tracking for assessment of cardiac motion and dyssynchrony," *Echocardiography*, vol. 25, no. 10, pp. 1167–1171, Oct. 2008.

[104] L. N. Bohs, B. J. Geiman, M. E. Anderson, S. C. Gebhart, and G. E. Trahey, "Speckle tracking for multi-dimensional flow estimation," *Ultrasonics*, vol. 38, nos. 1–8, pp. 369–375, Mar. 2000.

[105] J. Udesen, F. Gran, K. Hansen, J. A. Jensen, C. Thomsen, and M. B. Nielsen, "High frame-rate blood vector velocity imaging using plane waves: Simulations and preliminary experiments," *IEEE Trans. Ultrason., Ferroelectr., Freq. Control*, vol. 55, no. 8, pp. 1729–1743, Aug. 2008.

[106] M. Lenge, A. Ramalli, E. Boni, H. Liebgott, C. Cachard, and P. Tortoli, "High-frame-rate 2-D vector blood flow imaging in the frequency domain," *IEEE Trans. Ultrason., Ferroelectr., Freq. Control*, vol. 61, no. 9, pp. 1504–1514, Sep. 2014.

[107] R. S. Bandaru *et al.*, "Speckle tracking of tendon displacement in the carpal tunnel: Improved quantification using singular value decomposition," *IEEE J. Biomed. Health Informat.*, vol. 23, no. 2, pp. 817–824, Mar. 2019.

[108] J. Voorneveld *et al.*, "Native blood speckle vs ultrasound contrast agent for particle image velocimetry with ultrafast ultrasound-*in vitro* experiments," in *Proc. IEEE Int. Ultrason. Symp. (IUS)*, Sep. 2016, pp. 1–4.

[109] B. Baillargeon, N. Rebelo, D. D. Fox, R. L. Taylor, and E. Kuhl, "The living heart project: A robust and integrative simulator for human heart function," *Eur. J. Mech. A/Solids*, vol. 48, pp. 38–47, Nov. 2014.

[110] E. W. Weisstein. (2019). *Apodization Function*. [Online]. Available: http://mathworld.wolfram.com/ApodizationFunction.html

[111] C. Goffinet and J.-L. Vanoverschelde, "Speckle tracking echocardiography," *Eur. Cardiol. Rev.*, vol. 3, no. 1, pp. 1–3, 2007.

[112] J.-Y. Bouguet, "Pyramidal implementation of the affine Lucas Kanade feature tracker description of the algorithm," *Intel Corp.*, vol. 5, nos. 1–10, pp. 1–9, 2001.

[113] F. Sammali *et al.*, "Experimental setup for objective evaluation of uterine motion analysis by ultrasound speckle tracking," *Biomed. Phys. Eng. Express*, vol. 4, no. 3, Mar. 2018, Art. no. 035012.

[114] D. De Ziegler, C. Bulletti, R. Fanchin, M. Epiney, and P.-A. Brioschi, "Contractility of the nonpregnant uterus," *Ann. New York Acad. Sci.*, vol. 943, no. 1, pp. 172–184, Jan. 2006.

[115] C. Bulletti, D. de Ziegler, V. Polli, L. Diotallevi, E. D. Ferro, and C. Flamigni, "Uterine contractility during the menstrual cycle," *Hum. Reproduction*, vol. 15, no. suppl 1, pp. 81–89, Jun. 2000.

[116] M. M. Ijland, J. L. H. Evers, G. A. J. Dunselman, and H. J. Hoogland, "Subendometrial contractions in the nonpregnant uterus: An ultrasound study," *Eur. J. Obstetrics Gynecol. Reproductive Biol.*, vol. 70, no. 1, pp. 23–24, Dec. 1996.

[117] Y. L. Li, D. Hyun, L. Abou-Elkacem, J. K. Willmann, and J. J. Dahl, "Visualization of small-diameter vessels by reduction of incoherent reverberation with coherent flow power Doppler," *IEEE Trans. Ultrason., Ferroelectr., Freq. Control*, vol. 63, no. 11, pp. 1878–1889, Nov. 2016.

[118] J. S. Turek, M. Elad, and I. Yavneh, "Clutter mitigation in echocardiography using sparse signal separation," *Int. J. Biomed. Imag.*, vol. 2015, Jun. 2015, Art. no. 958963.

[119] M. Zibulevsky and B. A. Pearlmutter, "Blind source separation by sparse decomposition in a signal dictionary," *Neural Comput.*, vol. 13, no. 4, pp. 863–882, 2001.

[120] P. Li, X. Yang, D. Zhang, and Z. Bian, "Adaptive clutter filtering based on sparse component analysis in ultrasound color flow imaging," *IEEE Trans. Ultrason., Ferroelectr., Freq. Control*, vol. 55, no. 7, pp. 1582–1596, Jul. 2008.